Bioresource Technology 207 (2016) 409–421

Contents lists available at ScienceDirect

Bioresource Technology

journal homepage: www.elsevier.com/locate/biortech

Thermochemical conversion of biomass in smouldering combustion across scales: The roles of heterogeneous kinetics, oxygen and transport phenomena

Xinyan Huang, Guillermo Rein *

Department of Mechanical Engineering, Imperial College London, United Kingdom

HIGHLIGHTS

- Based on TGA, 3-, 5- and 9-step kinetics are proposed for biomass smouldering.
- The order of biomass oxidation is determined, which is less than one.
- 5-Step kinetics is suitable for biomass smouldering under various X_{O2} and scales.
- Proposed 1D model predicts burning rates in bench-scale biomass smouldering.
- Stochastic sensitivity analysis is applied to test model accuracy and reliability.

GRAPHICAL ABSTRACT

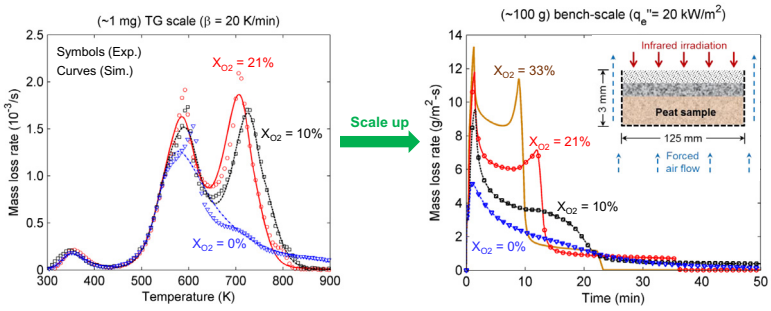

ARTICLE INFO

Article history:
Received 11 November 2015
Received in revised form 5 January 2016
Accepted 6 January 2016
Available online 22 January 2016

Keywords:
Pyrolysis
Oxidation
Thermogravimetry
Computational
Heat and mass transfer

ABSTRACT

The thermochemical conversion of biomass in smouldering combustion is investigated here by combining experiments and modeling at two scales: matter (1 mg) and bench (100 g) scales. Emphasis is put on the effect of oxygen (0–33 vol.%) and oxidation reactions because these are poorly studied in the literature in comparison to pyrolysis. The results are obtained for peat as a representative biomass for which there is high-quality experimental data published previously. Three kinetic schemes are explored, including various steps of drying, pyrolysis and oxidation. The kinetic parameters are found using the Kissinger–Genetic Algorithm method, and then implemented in a one-dimensional model of heat and mass transfer. The predictions are validated with thermogravimetric and bench-scale experiments and then analyzed to unravel the role of heterogeneous reaction. This is the first time that the influence of oxygen on biomass smouldering is explained in terms of both chemistry and transport phenomena across scales.

1. Introduction

Biomass is a solid fuel of natural origin that can present very high moisture and mineral contents (McKendry, 2002). Once heated, biomass dries and pyrolyzes (Anca-Couce, 2016), and if oxygen is present, it can ignite and support gas-phase homogenous combustion (flaming) or heterogeneous combustion (smouldering) (Ohlemiller, 1985; Rein, 2016). While most studies of biomass combustion have focused on flaming, this paper focuses on smouldering.

Smouldering is the slow, low-temperature, flameless burning of porous fuels and the most persistent type of combustion (Rein et al., 2006). The thermochemical process in smouldering includes drying, pyrolysis and oxidation steps (Ohlemiller, 1985; Huang and Rein, 2014). Therefore, compared to biomass pyrolysis (Di Blasi,

* Corresponding author. Tel.: +44 (0)20 7594 7036.
E-mail address: g.rein@imperial.ac.uk (G. Rein).

http://dx.doi.org/10.1016/j.biortech.2016.01.027
0960-8524/

Nomenclature

c	heat capacity
d_p	characteristic pore size
E	activation energy
h	enthalpy
h_c	convective coefficient
h_m	mass-transfer coefficient
ΔH	heat of reaction
k	thermal conductivity
K	permeability
L	sample size
$\dot{m}''$	mass flux
n	reaction order
P	pressure
$\dot{q}''_e$	irradiation
$\dot{q}''_r$	in-depth irradiation
R	gas constant
S	particle surface area
t	time
T	temperature
X	volume fraction
Y	mass fraction
z	distance
Z	pre-exponential factor

Greek

β	heating rate
γ	radiative coefficient
δ	thickness
ε	emissivity
κ	radiation absorption coefficient
ν	stoichiometric coefficient
ρ	bulk density
σ	Stefan–Boltzmann const.
χ	fraction factor
ψ	porosity
$\dot{\omega}$	reaction rate

Superscripts

$*$	critical or normalized

Subscripts

0	initial
∞	ambient condition
α	α-char
β	β-char
a	ash
b	biomass
c	cellulose
d	destruction
dr	drying
f	formation
g	gas
h	hemicellulose
i	condensed species index
j	gaseous species index
k	reaction index
l	lignin
o	oxidation
p	peat species, or pyrolysis reaction
s	solid
sm	smouldering
w	water

2008; Anca-Couce, 2016), smouldering is more complex and poorly studied. Particularly, biomass smouldering plays an important role in cooking fuels, biochar production, incineration of biowaste, fire hazards and wildfires (Carvalho et al., 2002; Blasi et al., 2004; Rein, 2013).

From a chemical point of view, biomass is a natural composite material, constituted by a mixture of three main components: hemicellulose (H), cellulose (C) and lignin (L) (Di Blasi, 1993; Ding et al., 2016; Anca-Couce, 2016). Neglecting the small amounts of extractives and other species, biomass composition can be approximated as:

$$\text{biomass} \approx Y_h\text{H} + Y_c\text{C} + Y_l\text{L} \quad (1)$$

where Y_i represents the mass fraction of component i. Fig. 1 compares thermogravimetric (TG) data for a series of biomass types under inert or oxidative atmospheres (Niu, 2014; Su et al., 2012; Zhao et al., 2014). A clear similarity in the decomposition process can be observed for pine needle, pine wood, forest peat and moss peat samples. Such similarity implies that there could be a general kinetic scheme to describe biomass thermochemical conversion in both inert and oxidative atmospheres.

Most studies in the literature investigate biomass kinetics using very small samples, at the 1 mg scale, in thermogravimetric (TG) experiments under either inert ambient or air, e.g. Huang and Rein (2014) and Ding et al. (2016). Fewer studies conducted TG experiments under other oxygen concentrations (X_{O_2}, percentage by volume). For example, Zhao et al. (2014) found that as the oxygen concentration decreased to sub-atmospheric levels, the mass-loss rate of biomass decreased. Amutio et al. (2012) proposed a 6-step kinetics to explain the oxidative pyrolysis of lignocellulosic biomass. Anca-Couce et al. (2012) proposed 3- and 7-step kinetic schemes to explain the TG data of wood under sub-atmospheric oxygen levels. However, studies at the TG scale alone do not provide in-sight about the changing role of chemistry at larger scales where heat and mass transfer processes are also important.

This paper chooses peat as a representative biomass because the literature offers high-quality experimental data in both TG and bench scales. Peat is an organic soil formed through incomplete humification processes of various dead plants. It is porous and forms a char upon heating, thus peat is prone to smouldering combustion (Rein, 2016). Smouldering megafires of peatlands are a very important source of greenhouse gases, and result in the widespread destruction of valuable ecosystems and large regional haze events (Turetsky et al., 2015). Several bench-scale (~100 g) experiments have studied the influence of oxygen on peat smouldering. Belcher et al. (2010) found that in laboratory scale experiments, smouldering could not be sustained for peat below a critical X_{O_2} of 16%. Hadden et al. (2013) found that smouldering of dry moss peat (MC $\leq$ 10% and IC $\approx$ 2%[1]) exposed to wind could be initiated by an irradiation of 20 kW/m^2 within 1 min under X_{O_2} as low as 11%. In a previous study (Huang and Rein, 2014), a 5-step kinetic scheme (including drying) was proposed and successfully explained

[1] Moisture content (MC) is defined here in dry basis as the mass of water divided by the mass of a dried soil sample, expressed as %. Inorganic or inert content (IC) is defined here in dry basis as the mass of soil inorganic matter (minerals) divided by the mass of a dried soil sample, expressed as %.

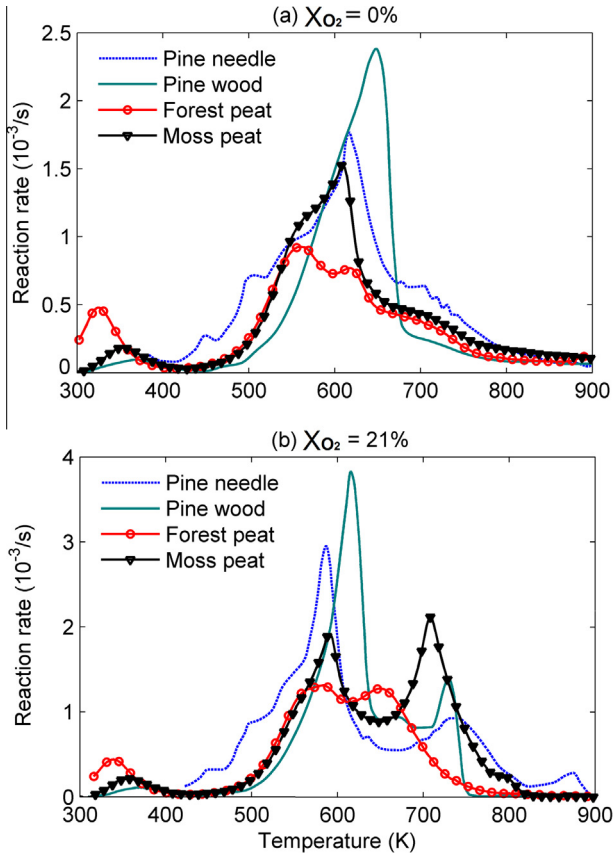

Fig. 1. Comparison of thermogravimetric mass-loss rates (DTG) at 20 K/min for pine needle (Niu, 2014), pine wood (Su et al., 2012), forest peat soil (Zhao et al., 2014) and moss peat soil in this study under (a) inert (X_{O_2} = 0%), and (b) air (X_{O_2} = 21%) atmospheres.

all TG data of peat under both inert and air atmospheres, but did not address the effect of oxygen concentration at levels different from the current atmospheric level. This kinetic scheme was implemented in a one-dimensional (1D) model of heat and mass transfer, and was shown to successfully predict bench-scale experiments in air (Huang et al., 2015; Huang and Rein, 2015).

In this work, three kinetic schemes of different complexities for the thermochemical conversion of biomass in smouldering are studied first. TG data of two peat is chosen, and their kinetic parameters are found via Kissinger–Genetic Algorithm (K–GA) method. Afterwards, a 1D model, including kinetics as well as heat and mass transfer, is developed to simulate a bench-scale experiments with dry peat samples under oxygen- or nitrogen-enriched atmospheres. Modeling results are compared with the experiments in Hadden (2011) and Hadden et al. (2013), and the model sensitivity to physico-chemical properties is investigated. This is the fist time that biomass smouldering is studied computationally under both sub- and super-atmospheric oxygen levels, and in both TG and bench scales.

2. Kinetic model

2.1. Moisture content and drying

When biomass is heated, water vaporizes below 400 K, denoted by the first peak in the first derivative of TG data (DTG curve), as seen in Fig. 1. If MC is low, there is no free or capillary water, while water molecules are absorbed into the porous matrix by hydrogen bond, i.e. the bound water (<10 vol.%) (Punmia and Jain, 2005). The drying of bound water in biomass can be described by a single dissociation step, as shown in Huang and Rein (2014)

$$\text{biomass} \cdot \nu_{w,dr}H_2O \rightarrow \text{biomass} + \nu_{w,dr}H_2O(g) \quad (dr) \tag{2}$$

where $\nu_{i,k}$ is the mass stoichiometric coefficient of species i in reaction k. In Eq. (2), $\nu_{w,dr} = MC_0$ is the initial moisture, and "·" means that water is bonded to biomass.

2.2. Pyrolysis

Pyrolysis is the thermochemical degradation of a solid without consumption of oxygen, which produces gases (pyrolysate), liquids (tar) and solids (char) (Di Blasi, 1993). For the pyrolysis of most biomass in an inert atmosphere, there is a clear peak in DTG curves after the drying region ($T > 400$ K), as seen in Fig. 1(a). Accordingly, biomass pyrolysis is often represented by a global 1-step reaction (Moussa et al., 1977; Ohlemiller, 1985) as

$$\text{biomass} \rightarrow \nu_{\alpha,bp}\alpha\text{-char} + \nu_{g,bp}\text{gas} \quad (bp) \tag{3}$$

which has been widely used for wood, peat and biowaste (Di Blasi, 1993; McKendry, 2002; Di Blasi, 2008; Huang and Rein, 2014; Li et al., 2014).

If biomass is viewed as a mixture of hemicellulose, cellulose and lignin as Eq. (1), its pyrolysis becomes a group of parallel reactions, each of which is the pyrolysis of one component. This kind of pyrolysis mechanism was proposed by Di Blasi (1993) as

$$\begin{cases} H \rightarrow \nu_{\alpha,hp}\alpha\text{-char} + \nu_{g,hp}\text{gas} & (hp) \\ C \rightarrow \nu_{\alpha,cp}\alpha\text{-char} + \nu_{g,cp}\text{gas} & (cp) \\ L \rightarrow \nu_{\alpha,lp}\alpha\text{-char} + \nu_{g,lp}\text{gas} & (lp) \end{cases} \tag{4}$$

where the same α-char is assumed to produced in each pyrolysis reaction.

2.3. Oxidation

For biomass decomposing in an oxidative atmosphere like air, there is another clear peak at temperatures above the pyrolysis region in DTG curves, as shown in Fig. 1(b). Therefore, at least one oxidation reaction takes place at higher temperature, *i.e.* char oxidation (Rein et al., 2006) as

$$\alpha\text{-char} + \nu_{O_2,\alpha o}O_2 \rightarrow \nu_{a,\alpha o}\text{ash} + \nu_{g,\alpha o}\text{gas} \quad (\alpha o) \tag{5}$$

Moussa et al. (1977) proposed using one pyrolysis plus one char oxidation (2-step) to simulate the smouldering process of cellulosic materials. It is so far the simplest scheme to describe the chemical process of smouldering, and has been used for many biomass types (Ohlemiller, 1985; Di Blasi, 1993; Anca-Couce et al., 2012; Huang and Rein, 2014).

The comparison between Fig. 1(a) and (b) shows that for each biomass, the second peak right after the drying region (400 K < T < 650 K) is earlier and higher in air than in inert atmospheres. This shows that the presence of oxygen significantly alters the conversion. Ohlemiller (1985) first proposed a parallel fuel oxidation in smouldering as

$$\text{biomass} + \nu_{O_2,bo}O_2 \rightarrow \nu_{\beta,bo}\beta\text{-char} + \nu_{g,bo}\text{gas} \quad (bo) \tag{6}$$

where a different type of β-char is produced. Compared to α-char from pyrolysis in Eq. (3), this β-char is yielded through a different thermochemical process consuming oxygen, so in general they have different structures, compositions, and reactivities. Recently, Huang and Rein (2014) found that for peat, a single char-oxidation is not sufficient to explain TG data at high temperature ($T > 700$ K).

Therefore, it is assumed here that β-char goes through a parallel oxidation into ash as

$$\beta\text{-char} + \nu_{O_2,\beta o}O_2 \rightarrow \nu_{a,\beta o}\text{ash} + \nu_{g,\beta o}\text{gas} \qquad (\beta o) \tag{7}$$

This 5-step scheme (including drying and assuming first order oxidation) successfully explained TG data of four different peat types in a previous study (Huang and Rein, 2014).

On the other hand, TG experiments (Amutio et al., 2012; Anca-Couce et al., 2012) had shown that each component in biomass can go through a parallel oxidization simultaneously, same as the parallel pyrolysis. Thus, the biomass oxidation can be proposed as

$$\begin{cases} H + \nu_{O_2,ho}O_2 \rightarrow \nu_{\beta,ho}\beta\text{-char} + \nu_{g,ho}\text{gas} & (ho) \\ C + \nu_{O_2,co}O_2 \rightarrow \nu_{\beta,co}\beta\text{-char} + \nu_{g,co}\text{gas} & (co) \\ L + \nu_{O_2,lo}O_2 \rightarrow \nu_{\beta,lo}\beta\text{-char} + \nu_{g,lo}\text{gas} & (lo) \end{cases} \tag{8}$$

where the same β-char is assumed from all three oxidation reactions.

In summary, three possible kinetic schemes (including drying) are proposed for biomass smouldering as

(I) 3-step scheme

$$\begin{cases} \text{biomass} \cdot \nu_{w,dr}H_2O \rightarrow \text{biomass} + \nu_{w,dr}H_2O(g) & (dr) \\ \text{biomass} \rightarrow \nu_{\alpha,pp}\alpha\text{-char} + \nu_{g,pp}\text{gas} & (bp) \\ \alpha\text{-char} + \nu_{O_2,\alpha o}O_2 \rightarrow \nu_{a,\alpha o}\text{ash} + \nu_{g,\alpha o}\text{gas} & (\alpha o) \end{cases} \tag{9}$$

(II) 5-step scheme

$$\begin{cases} \text{biomass} \cdot \nu_{w,dr}H_2O \rightarrow \text{biomass} + \nu_{w,dr}H_2O(g) & (dr) \\ \text{biomass} \rightarrow \nu_{\alpha,pp}\alpha\text{-char} + \nu_{g,pp}\text{gas} & (bp) \\ \text{biomass} + \nu_{O_2,po}O_2 \rightarrow \nu_{\beta,po}\beta\text{-char} + \nu_{g,po}\text{gas} & (bo) \\ \beta\text{-char} + \nu_{O_2,\beta o}O_2 \rightarrow \nu_{a,\beta o}\text{ash} + \nu_{g,\beta o}\text{gas} & (\beta o) \\ \alpha\text{-char} + \nu_{O_2,\alpha o}O_2 \rightarrow \nu_{a,\alpha o}\text{ash} + \nu_{g,\alpha o}\text{gas} & (\alpha o) \end{cases} \tag{10}$$

(III) 9-step scheme

$$\begin{cases} \text{biomass} \cdot \nu_{w,dr}H_2O \rightarrow \text{biomass} + \nu_{w,dr}H_2O(g) & (dr) \\ H \rightarrow \nu_{\alpha,hp}\alpha\text{-char} + \nu_{g,hp}\text{gas} & (hp) \\ C \rightarrow \nu_{\alpha,cp}\alpha\text{-char} + \nu_{g,cp}\text{gas} & (cp) \\ L \rightarrow \nu_{\alpha,lp}\alpha\text{-char} + \nu_{g,lp}\text{gas} & (lp) \\ H + \nu_{O_2,ho}O_2 \rightarrow \nu_{\alpha,hp}\beta\text{-char} + \nu_{g,hp}\text{gas} & (ho) \\ C + \nu_{O_2,co}O_2 \rightarrow \nu_{\alpha,cp}\beta\text{-char} + \nu_{g,cp}\text{gas} & (co) \\ L + \nu_{O_2,lo}O_2 \rightarrow \nu_{\alpha,lp}\beta\text{-char} + \nu_{g,lp}\text{gas} & (lo) \\ \beta\text{-char} + \nu_{O_2,\beta o}O_2 \rightarrow \nu_{a,\beta o}\text{ash} + \nu_{g,\beta o}\text{gas} & (\beta o) \\ \alpha\text{-char} + \nu_{O_2,\alpha o}O_2 \rightarrow \nu_{a,\alpha o}\text{ash} + \nu_{g,\alpha o}\text{gas} & (\alpha o) \end{cases} \tag{11}$$

where for parallel reactions, e.g. $A \rightarrow \nu_B B \rightarrow \nu_a$ ash, and $A \rightarrow \nu_C C \rightarrow \nu_a$ ash, the mass of ash (or IC) is conserved as

$$\nu_B \nu_a = \nu_C \nu_a = \text{IC}_A \tag{12}$$

2.4. Reaction rate

The general heterogeneous reaction, k, in the mass basis can be written (Lautenberger and Fernandez-Pello, 2009) as

$$A_k + \sum_{j=1}^{N} \nu'_{j,k}\ \text{gas}\ j \rightarrow \nu_{B,k}B_k + \sum_{j=1}^{N} \nu''_{j,k}\text{gas}\ j \tag{13}$$

For a small biomass particle sample of initial mass m_0 and uniform temperature T, the non-dimensional decomposition rate of species A ($\dot{\omega}^*_{dA_k} > 0$) is expressed by the Arrhenius-type reaction as

$$\dot{\omega}^*_{dA_k} = Z_k \exp\left(-\frac{E_k}{RT}\right) f(m^*_A) g(Y_{O_2}) \tag{14}$$

where Z_k and E_k are the pre-exponential factor and the activation energy, respectively; and $f(m^*_A)$ and $g(Y_{O_2})$ are the mass action functions of reactant A and oxygen, respectively.

Both $\dot{\omega}^*_k$ and $m^*_{dA_k}$ are non-dimensionalized to a characteristic mass of the cell. Here, m_A is non-dimensionalized to the source species for the reactant A as

$$m^*_A = \frac{m_A}{m_{sA0}} \tag{15}$$

where the subscript "$sA0$" represents the initial mass of source species for A. For example, the source species for water is water; and the source species for cellulose, char or ash is the original biomass. Non-dimensionalizing to the source species allows avoiding the interference among parallel reactions, and is especially suitable to model complex and heterogeneous mixtures like biomass (see conversions to other reaction-rate expressions in Appendix A.1).

The nth-order mass action function is chosen for reactant A as

$$f(m^*_A) = (m^*_A)^{n_k} = \left(\frac{m_A}{m_{sA0}}\right)^{n_k} \tag{16}$$

where n_k is called as the order of reaction k. The mode for oxygen is chosen as

$$g(Y_{O_2}) = \begin{cases} 1 & \text{(inert atmosphere)} \\ (1 + Y_{O_2})^{n_{O_2,k}} - 1 & \text{(oxidative atmosphere)} \end{cases} \tag{17}$$

where $n_{O_2,k}$ is the order of oxidation. In inert atmosphere ($Y_{O_2} = 0$), oxidation reaction rates are zero. Therefore, the dimensional expressions for the destruction rate of A, formation rate of B, and heat release rate for reaction k are

$$\begin{cases} \dot{\omega}_{dA_k} & = \dot{\omega}^*_{dA_k} m_{sA0} \\ \dot{\omega}_{fB_k} & = \dot{\omega}^*_{dA_k} \nu_{B,k} m_{sA0} \\ \dot{Q}_k & = \dot{\omega}_{dA_k} \Delta H_k \end{cases} \tag{18}$$

where subscripts "d" and "f" represent the destruction and the formation, respectively, and ΔH_k is the heat of reaction.

3. Results of modeling TG experiments

3.1. Thermogravimetric experiment

TG experiments are the most widely used technique to study solid-phase kinetics. It provides an environment of controlled atmosphere and heating rate, and small thermal gradient and transport effects during degradation of samples. Here, TG experiments of two peat types are studied. One sample is a commercial Shamrock moss peat (Bord na Móna Horticulture Ltd.) from Ireland. This low-mineral (IC $\approx 2\%$) moss peat is the same peat used in Belcher et al. (2010), Hadden (2011) and Hadden et al. (2013), and details are presented here. The other peat sample is from the forest of Changpai Mountains in Northeast China. TG data of this high-mineral (IC $\approx 22\%$) forest peat under 0–21% X_{O_2} was reported in Zhao et al. (2014). This forest peat is analyzed in the same way as the moss peat, and details are presented in Appendix B.1.

The moss peat sample was pulverized into powders and dried at 90 °C for 48 h. A Shimadzu DTG-60H TG analyzer was used. The initial mass of peat was 3.5 mg and samples were heated at three constant rates of 10, 20, and 30 K/min. Three oxygen concentrations were selected, 0% (helium), 10%, and 21% (air), with a flow rate of 50 mL/min. Experiments were repeated twice for each case, showing a good repeatability (uncertainty $\approx 2\%$). Fig. 2 shows the mass-loss rate (DTG) curves of this low-mineral moss peat soil.

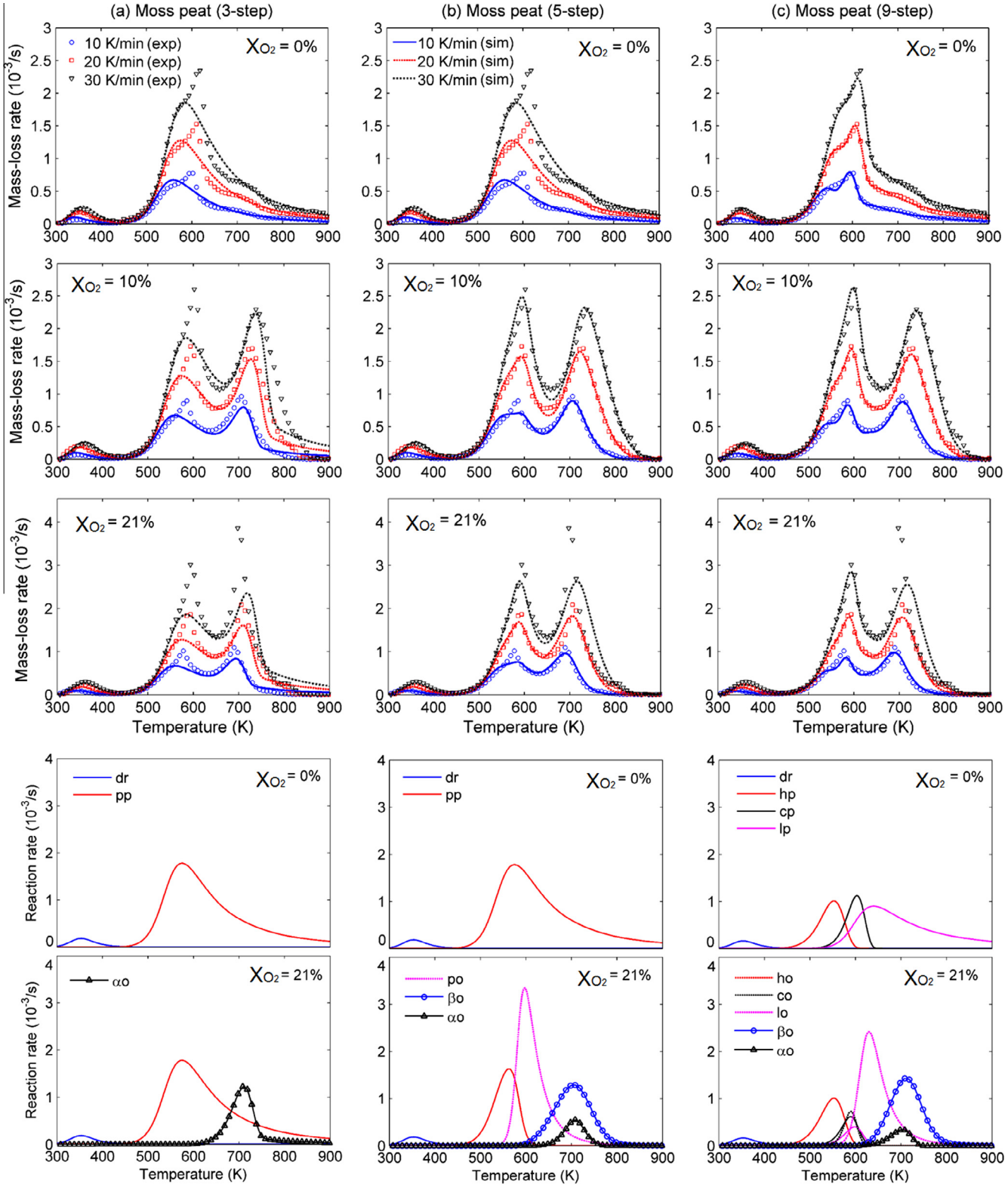

Fig. 2. Measured and predicted DTG curves, and the predicted reaction rates of the low-mineral moss peat under different oxygen concentrations (X_{O_2}) by (a) 3-step, (b) 5-step, and (c) 9-step kinetic scheme.

3.2. K–GA method

The small sample in TG experiment can be assumed to be a lumped capacitance, and the normalized mass-loss rate can be modeled as

$$\frac{dm}{dT} = \frac{dt}{dT}\sum_{i=1}^{N}\frac{dm_i}{dt} = \frac{1}{\beta}\sum_{i=1}^{N}(\dot{\omega}_{f,i} - \dot{\omega}_{d,i}) \tag{19}$$

where $\beta = dT/dt$ is the heating rate.

The recent Kissinger–Genetic Algorithm (K–GA) method (Li et al., 2014) is used here to quickly and accurately find good kinetic parameters to match the TG data as an inverse problem (Rein et al., 2006). First, Kissinger's method is used with TG data of multiple heating rates to find approximate values of Z_k and E_k for 1-step drying and 1-step pyrolysis. These approximate values are used to narrow the search range in Genetic Algorithm (GA). GA is a heuristic search method, imitating the principles of biological adaption based on Darwinian survival-of-the-fittest theory. GA is applied to couple with Eqs. (14), (18) and (19) to search for all kinetic and stoichiometric parameters.

In this work, the optimized parameters include the initial mass fractions (Y_{i0}) of each species, the kinetic triplets (Z_k, E_k, and n_k), yields ($\nu_{i,k}$), and the order of oxidation ($n_{O_2,k}$). The number of optmized parameters for 3-, 5- and 9-step schemes are 13, 22 and 40, respectively. In order to accelerate the optimization, parameters for drying and pyrolysis are optimized first with only TG data at inert atmosphere. Then, the remaining parameters of oxidation reactions are optimized with TG data at oxidative atmospheres.

The optimization target of the inverse problem is to minimize the error with respect to TG data, defined as

$$\Phi = \gamma \frac{\sum |\dot{m}_{pre,i} - \dot{m}_{exp,i}|}{\sum \dot{m}_{exp,i}} + (1-\gamma) \frac{\sum |m_{pre,i} - m_{exp,i}|}{\sum m_{exp,i}} \quad (20)$$

where summations means evaluating all TG data points; subscripts "*exp*" and "*pre*" denote the experimental and predicted results; and $\gamma = 0.5$ as used previously in Rein et al. (2006) and Huang and Rein (2014). In general, the population size in GA is set around 200, and the convergence ($\Delta\Phi < 0.1\%$) occurred after less than 1000 generations. The GA module in MATLAB is used.

3.3. Predicted TG data and kinetic parameters

For the low-mineral moss peat, 9 sets of TG data are available: 3 oxygen concentrations × 3 heating rates. 7 sets are chosen for optimization. Then, these optimized parameters are used to predict blindly another 2 sets of TG data: (1) $X_{O_2} = 0\%$ at 10 K/min and (2) $X_{O_2} = 21\%$ at 30 K/min. The best values found are listed in Tables 1 (3- and 5-step) and (9-step in Appendix B). Table 2 summarizes the overall error in both optimization and blind prediction for each kinetic scheme. All experimental and predicted TG curves as well as the predicted reaction rates at 20 K/min in $X_{O_2} = 0\%$ and 21% are compared in Fig. 2.

Fig. 2 show that all three kinetics schemes are able to produce three major DTG peaks in all heating rates and oxygen concentrations. More importantly, based on this extensive TG data set under various oxygen concentrations, the order of oxidation ($n_{O_2,k}$) is determined here, instead of assuming its value, e.g. assuming first order ($n_{O_2,k} = 1$) in Lautenberger and Fernandez-Pello (2009), Amutio et al. (2012), and Huang and Rein (2014). Tables 1 and B1 show that for both peat samples $n_{O_2,k} < 1$ is found for all oxidation reactions in all three kinetic schemes, similar to found values

Table 1
Kinetic parameters for the low-mineral moss peat and high-mineral forest peat samples with the 3- and 5-step schemes (including 1-step drying). $\Delta H > 0$ (endothermic); $\Delta H < 0$ (exothermic).

Parameter	Moss peat	Range	Forest peat	Range	Unit
MC	4.1	[2.9, 4.2]	9.0	[7.8, 9.2]	%
IC	2.1	[2.1, 2.3]	22.2	[21.8, 22.5]	%
3-step					
$\lg A_{dr}$	6.91	[6.62, 7.35]	7.27	[7.10, 8.79]	$\lg(s^{-1})$
E_{dr}	58.7	[56.9, 61.5]	58.6	[57.8, 67.9]	kJ/mol
n_{dr}	2.37	[2.25, 2.53]	2.60	[2.56, 2.72]	–
ΔH_{dr}	2.26	–	2.26	–	MJ/kg
$\lg A_{pp}$	8.18	[6.01, 8.18]	6.85	[6.61, 7.13]	$\lg(s^{-1})$
E_{pp}	112	[89.9, 112]	99.2	[97.2, 101]	kJ/mol
n_{pp}	5.31	[3.12, 5.31]	5.67	[5.19, 5.67]	–
$\nu_{\alpha,pp}$	0.28	[0.28, 0.36]	0.40	[0.38, 0.40]	kg/kg
ΔH_{pp}	0.5	–	0.5	–	MJ/kg
$\lg A_{\alpha o}$	10.2	[0.17, 11.4]	3.99	[3.99, 6.84]	$\lg(s^{-1})$
$E_{\alpha o}$	160	[139, 170]	67.8	[67.8, 93.7]	kJ/mol
$n_{\alpha o}$	0.51	[0.51, 1.21]	0.47	[0.39, 1.92]	–
$n_{O_2,\alpha o}$	0.86	[0.80, 0.96]	0.59	[0.38, 0.91]	–
$\nu_{a,\alpha o}$	0.01	[0.009,0.01]	0.24	[0.24, 0.41]	kg/kg
$\Delta H_{\alpha o}$	−29.7	–	−15.1	–	MJ/kg
5-step[b]					
$\lg A_{po}$	16.8	[12.0, 16.8]	6.63	[6.35, 7.38]	$\lg(s^{-1})$
E_{po}	195	[142, 195]	89.2	[86.0, 96.7]	kJ/mol
n_{po}	2.33	[1.68, 2.40]	1.86	[1.63, 2.00]	–
$n_{O_2,po}$	0.24	[0.23, 0.26]	0.55	[0.50, 0.58]	–
$\nu_{\beta,po}$[a]	0.61	[0.61, 0.63]	0.39	[0.36, 0.44]	kg/kg
ΔH_{po}	−11.6	–	−12.3	–	MJ/kg
$\lg A_{\beta o}$	7.38	[7.28, 8.27]	14.4	[9.87, 15.3]	$\lg(s^{-1})$
$E_{\beta o}$	117	[113, 124]	181	[136, 190]	kJ/mol
$n_{\beta o}$	1.32	[1.19, 1.32]	2.26	[1.42, 2.45]	–
$n_{O_2,\beta o}$	0.52	[0.47, 0.62]	0.54	[0.51, 0.72]	–
$\nu_{a,\beta o}$	0.04	[0.03, 0.04]	0.62	[0.55, 0.65]	–
$\Delta H_{\beta o}$	−28.9	–	−7.6	–	MJ/kg
$\lg A_{\alpha o}$	13.3	[12.0, 13.7]	10.1	[9.97, 14.2]	$\lg(s^{-1})$
$E_{\alpha o}$	172	[158, 175]	143	[142, 176]	kJ/mol
$n_{\alpha o}$	2.58	[2.38, 2.83]	1.31	[1.23, 3.44]	–
$n_{O_2,\alpha o}$	0.86	[0.85, 0.96]	0.86	[0.81, 1.09]	–
$\nu_{a,\alpha o}$	0.07	[0.07, 0.08]	0.59	[0.59, 0.61]	kg/kg
$\Delta H_{\alpha o}$	−27.8	–	−8.1	–	MJ/kg

[a] Calculated from Eq. (12).
[b] Drying and pyrolysis parameters of 5-step scheme are the same as 3-step scheme.

Table 2
The minimum error (Φ) after optimization and blind prediction of TG data for forest and moss peat.

Error (%)	3-step		5-step		9-step	
	Forest	Moss	Forest	Moss	Forest	Moss
Φ_{opt}	7.9	8.7	5.5	5.5	5.0	4.2
Φ_{pre}	16.7	16.5	10.5	11.0	10.0	9.0

for wood (Anca-Couce et al., 2012) and coal (Cozzani, 2000; Wu et al., 2015). This shows that the influence of oxygen in biomass smouldering is weaker than the widely assumed first order.

Comparison between 3-step and 5-step schemes shows that 5-step scheme gives a substancial improvement in both the optimized and blind predictions. Specifically, Table 2 shows that for both peat samples the minimum error for the optimization (Φ_{opt}) decreases from about 8% to 5.5%, and for the blind prediction (Φ_{pre}) decreases from 17% to 11%. Although the 9-step scheme improves TG prediction in inert atmosphere, there is only 0.5–2% reduction of the error. Moreover, Table 2 shows that the overall difference in predicting TG data between the 5-step and 9-step schemes is smaller than the expected uncertainty of TG experiment (2%). Therefore, it is questionable whether the added complexity of the 9-step scheme is justified for modelling purposes (Bal and Rein, 2013).

4. Modeling bench-scale smouldering experiments

The chemical validity of the schemes is investigated outside the TG realm in this section. Three kinetic schemes are incorporated into a 1D heat and mass transfer model to study the reaction and the species distribution inside a peat smouldering front.

In order to isolate the effect of biomass moisture and focus on the effect of oxygen, Hadden (2011) used oven-dried peat

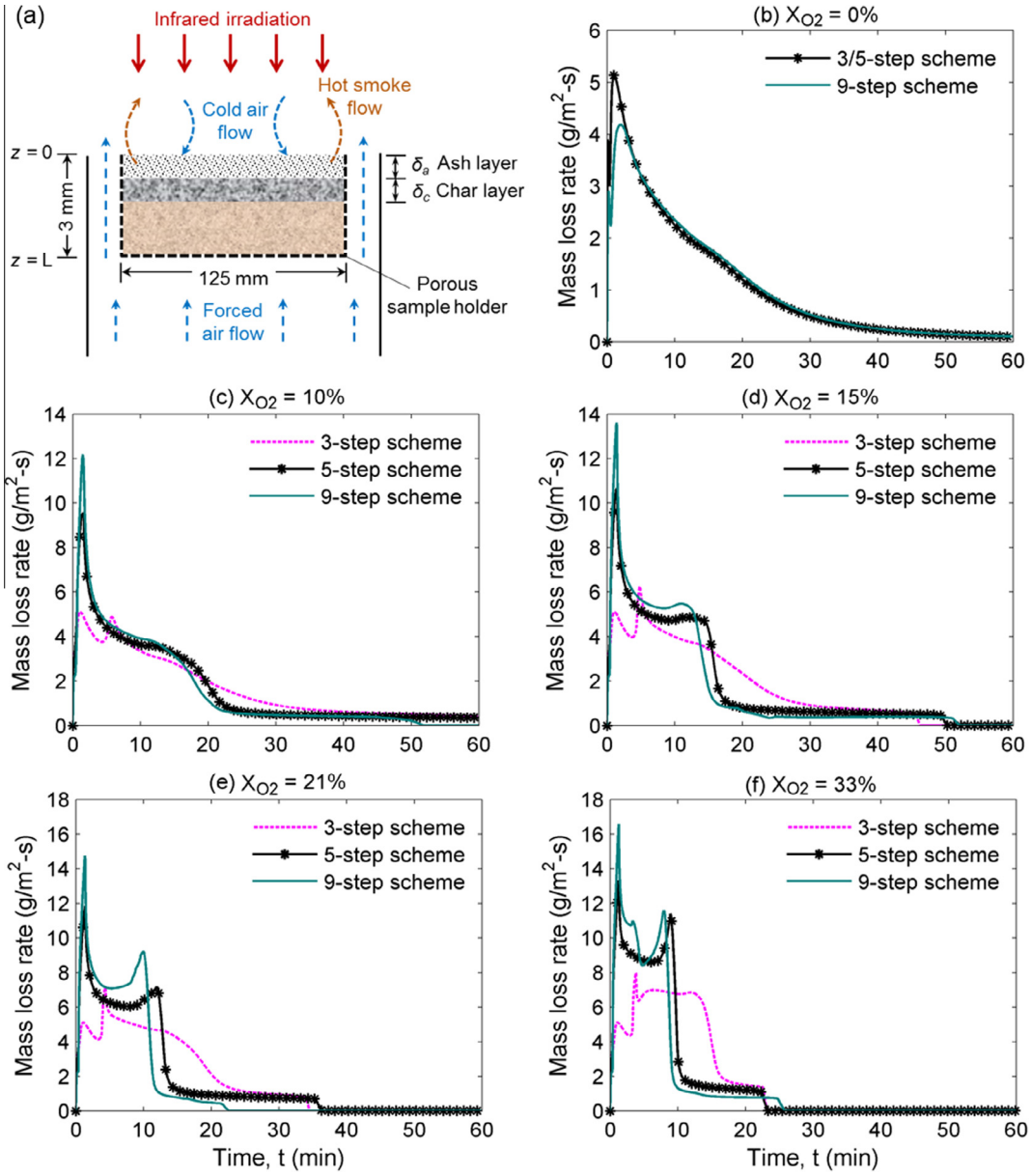

Fig. 3. (a) Sketch of bench-scale (~100 g) experimental setup in Hadden (2011) and Hadden et al. (2013) and the corresponding computational domain; predicted bench-scale mass-loss rate by 3-, 5- and 9-step schemes for moss peat under atmospheres of (b) N_2 (X_{O_2} = 0%), (c) X_{O_2} = 10%, (d) X_{O_2} = 15%, (e) air (X_{O_2} = 21%), and (f) X_{O_2} = 33% under an irradiation $\dot{q}''_e = 20$ kW/m^2 during the entire experiment.

(MC ≈ 10%) which is same moss peat for the TG experiment in Fig. 2. Experiments were conducted under various oxygen concentrations (0 ~ 35%) within a bench-scale smouldering reactor (125 mm diameter and 30 mm height with 80 ± 3 g peat), as shown in Fig. 3a. The reactor walls were porous to allow gas diffusion into the sample. Ignition was on the top surface by infrared irradiation at flux levels of 7.5, 10 and 20 kW/m^2 for 1 min, 10 min and the entire experiment. More details about these experiments can be found in Hadden (2011). Unlike the (~1 mg) TG experiment, inside this (~100 g) thick sample, heat and mass transfer cannot be neglected.

4.1. Governing equations

The horizonal dimension of the sample is much larger than the vertical dimension, and both irradiation and gas flow are uniform at the top and bottom surfaces. Therefore, the smouldering spread can be approximated as 1D spread along the vertical direction (Fig. 3a). If the top ignition source is too weak or the oxygen concentration is too low, the smouldering front may not ignite or spread. If ignited, a smouldering front starts to spread downward vertically.

In previous work (Huang et al., 2015; Huang and Rein, 2015), the influence of MC on ignition and spread in atmospheric normal air ($X_{O_2} = 21\%$) had been studied with a 1D model established in the open-source code Gpyro (Lautenberger and Fernandez-Pello, 2009). Such model is improved with the non-first-order oxidation found in the previous section and in-depth irradiation to simulate current bench-scale experiments. This is the first time that the effect of oxygen on biomass smouldering is simulated. The model solves transient equations for both the condensed and gas phases. The governing equations include Eq. (21) for condensed-phase mass conservation, Eq. (25) for condensed-phase species conservation, Eq. (23) for energy conservation (assuming thermal equilibrium between condensed and gas phases), Eq. (24) for gas-phase mass conservation, Eq. (25) for gas-phase species conservation and Eq. (26) for gas-phase momentum conservation:

$$\frac{\partial \overline{\rho}}{\partial t} = -\dot{\omega}'''_{fg} \tag{21}$$

$$\frac{\partial(\overline{\rho} Y_i)}{\partial t} = \dot{\omega}'''_{fi} - \dot{\omega}'''_{di} \tag{22}$$

$$\frac{\partial(\overline{\rho h})}{\partial t} + \frac{\partial(\dot{m}'' h_g)}{\partial z} = \frac{\partial}{\partial z}\left(\overline{k}\frac{\partial T}{\partial z}\right) + \sum_{k=1}^{K}\left(-\dot{\omega}'''_{di,k}\right)\Delta H_k - \frac{\partial \dot{q}''_r}{\partial z} \tag{23}$$

$$\frac{\partial\left(\rho_g \overline{\psi}\right)}{\partial t} + \frac{\partial \dot{m}''}{\partial z} = \dot{\omega}'''_{fg} \tag{24}$$

$$\frac{\partial\left(\rho_g \overline{\psi} Y_i\right)}{\partial t} + \frac{\partial(\dot{m}'' Y_j)}{\partial z} = -\frac{\partial}{\partial z}\left(\overline{\psi}\rho_g D\frac{\partial Y_j}{\partial z}\right) + \dot{\omega}'''_{fj} - \dot{\omega}'''_{dj} \tag{25}$$

$$\dot{m}'' = -\frac{\overline{K}}{\nu}\frac{\partial P}{\partial z} \qquad (P = \rho_g R_s T) \tag{26}$$

A constant irradiation ($\dot{q}''_e$) of variable intensity and duration is applied as the ignition source. The in-depth radiation in Eq. (23) is considered as

$$\dot{q}''_r(z) = \overline{\varepsilon}\dot{q}''_e exp(-z/\kappa) \tag{27}$$

where $\kappa = 1000$ m is assumed (Bal and Rein, 2013). The boundary conditions on the top free surface ($z = 0$) are

$$\begin{cases} -\overline{k}\frac{\partial T}{\partial z}\big|_0 = -h_{c0}(T_0 - T_\infty) - \overline{\varepsilon}\sigma\left(T_L^4 - T_\infty^4\right) \\ -\overline{\psi}\rho_g D\frac{\partial Y_j}{\partial z}\Big|_0 = h_{m0}\left(Y_{j\infty} - Y_{j0}\right) \\ P_0 = P_\infty \end{cases} \tag{28}$$

where an empirical convection coefficient is used, $h_{c0} = 1.52\Delta T^{1/3} = 1.52(300)^{1/3} \approx 10$ W/m^2-K (Holman, 1989); and the heat-mass transfer analogy is used, $h_{m0} \sim h_{c0}/c_g \approx 10$ g/m^2-s. The environmental pressure (P_∞) and temperature (T_∞) are constant at 1 atm and 300 K, respectively.

Similar convective boundary conditions are imposed on the back free surface ($z = L$) as

$$\begin{cases} -\overline{k}\frac{\partial T}{\partial z}\big|_L = -h_{cL}(T_L - T_\infty) - \overline{\varepsilon}\sigma\left(T_L^4 - T_\infty^4\right) \\ -\overline{\psi}\rho_g D\frac{\partial Y_j}{\partial z}\Big|_L = h_{mL}\left(Y_{j\infty} - Y_{jL}\right) \\ P_L = P_\infty \end{cases} \tag{29}$$

where $h_{cL} = h_{c,0} = 10$ W/m^2-K with surface radiation ($\varepsilon = 0.95$) because the bottom wall is not insulated, and $h_{mL} = 2$ g/m^2-s is chosen because the bottom wall is porous (mesh porosity = 0.26).

Gpyro adopts a fully implicit method to solve Eqs. (21)–(29). Details about numerical solution methodology are reported in Lautenberger and Fernandez-Pello (2009). The sample height during spread is equal to the sum of the height of each cell, $H_t = \sum_{n=1}^{N}\Delta z_n$, which depends on the mass conservation and density, capturing the surface regression observed during experiment. Simulations were run with an initial cell size of $\Delta z = 0.1$ mm, and initial time step of 0.02 s. Reducing the cell size and time step by a factor of 2 gives little difference in results, so this discretisation is acceptable.

4.2. Parameter selection and stochastic sensitivity analysis

Each condensed-phase species is assumed to have constant and temperature-independent properties (e.g. bulk density, specific heat, and porosity) for the sake of simplicity and the lack of data in the literature. All gaseous species have unity Schmidt number, and equal diffusion coefficient and specific heat. The averaged properties in each cell are calculated by weighting the appropriate mass fraction (Y_i) or volume fraction (X_i) (Lautenberger and Fernandez-Pello, 2009; Huang and Rein, 2015).

The bulk densities of all species for this moss peat were measured in Hadden (2011). The properties of α-char and β-char are assumed to be the same. The solid ($\psi_i = 0$) thermo-physical properties, $\rho_{s,i}, k_{s,i}, c_i$ of peat, char, and ash are selected from Jacobsen et al. (2003), all listed in Table 3. Then, porosity can be calculated as

$$\psi_i = 1 - \frac{\rho_i}{\rho_{s,i}} \tag{30}$$

which is found to be high for peat ($\psi_p = 0.867$). Also, the peat sample is dried, so the small amount of bound water (MC ⩽ 10%) is assumed to stay in the pores of peat without volume expansion and the wet peat bulk density is estimated as $\rho = (1 + \mathrm{MC})\rho_p$.

The effective thermal conductivity includes the radiation across pores as

$$k_i = k_{s,i}(1 - \psi_i) + \gamma_i \sigma T^3 \tag{31}$$

where $\gamma_i = 10^{-4} \sim 10^{-3}$ m depends on the pore size as $\gamma_i \approx 3d_{p,i}$ (Yu et al., 2006). The average pore size relates to the particle surface

Table 3
Physical properties of condensed-phase species: ρ_{si}, k_{si}, and c_i are from Jacobsen et al., 2003, and ρ_{i0} is from Hadden (2011) and Hadden et al. (2013).

Species (i)	ρ_{si} $\left(\frac{kg}{m^3}\right)$	ρ_{i0} $\left(\frac{kg}{m^3}\right)$	ψ_{i0} (−)	k_{si} $\left(\frac{W}{m\cdot K}\right)$	c_i $\left(\frac{J}{kg\cdot K}\right)$
Water	1000	1000	0	0.6	4186
Peat	1500	200[a]	0.867	1.0	1840
α-Char	1300	185	0.962	0.26	1260
β-Char	1300	185	0.962	0.26	1260
Ash	2500	35	0.997	1.2	1380

[a] Bulk density of oven-dried peat (MC = 10%) is 200(1 + MC) = 220 kg/m^3.

Table 4
Physicochemical parameters studied in sensitivity analysis, and corresponding ranges for stochastic sampling. Four parameters are selected and 40 stochastic sampling are conducted at a time.

Parameter	Initial value	Sampling range	Unit
k_{sp}	1.0	[0.5, 1.5]	W/m-K
k_{sc}	0.26	[0.15, 0.4]	W/m-K
c_p	1840	[1.5, 2.2]	kJ/kg-K
ΔH_{pp}	0.5	[0.2, 1]	MJ/kg
$\lvert\Delta H_{O_2}\rvert$	30	[25, 35]	MJ/kg
$h_{m,0}$	10	[5, 15]	g/m^2-s

area as $d_{p,i} = 1/S_i\rho_i$ where $S_p = S_c = 0.05$ m^2/g and $S_a = 0.2$ m^2/g (de Jonge and Mittelmeijer-Hazeleger, 1996). The absolute permeability of peat is assumed to be independent of the permeating fluid (air in this case), and can be estimated (Punmia and Jain, 2005) as

$$K_i = 10^{-3} d_{p,i}^2 \sim 1/\rho_i^2 \tag{32}$$

which varies from 10^{-12} to 10^{-9} m^2, and decreases as the bulk density increases.

The three proposed kinetic schemes (3-, 5- and 9-step) for biomass smouldering are examined with this 1D model. The heat of pyrolysis is chosen as $\Delta H_{pp} = 0.5$ MJ/kg (endothermic); the heat of oxidation is assumed to relate to the oxidized organic matter as $\Delta H_k = \Delta H_{O_2}(1 - \nu_{B,k}) < 0$ (exothermic) (Huang et al., 2015). According to differential scanning calorimetry (DSC) of multiple peat samples (Bergner and Albano, 1993), $\Delta H_{O_2} = -30$ MJ/kg is estimated for the low-mineral moss peat, and $\Delta H_{O_2} = -20$ MJ/kg for high-mineral forest peat. The heat of reactions are listed in Tables 1 and B1, with overall smouldering heats of $|\Delta H_{sm}| = 18.7$ MJ/kg (moss peat) and $|\Delta H_{sm}| = 10.2$ MJ/kg (forest peat) in TG environment with air. The oxygen consumption is related to the heat of oxidation as $\nu_{O_2,k} = \Delta H_k/(-13.1\ \text{MJ/kg})$ (Huggett, 1980).

Fig. 3(b–f) compares the predicted moss-loss rate in bench-scale experiment by 3-, 5-, and 9-step schemes for moss peat under different oxygen concentrations. In inert atmosphere (Fig. 3b), the single pyrolysis reaction (Eq. (3)) in 3- and 5-step schemes gives a very similar prediction to three pyrolysis reactions (Eq. (4)) in 9-step scheme, despite small differences in the peak.

In the oxidative atmosphere cases (Fig. 3c–f), 3-step scheme predicts a relatively low mass-loss rate, different from 5- and 9-step predictions. This shows that the prediction error at TG scale can be significantly amplified at bench scale. Meanwhile, the prediction difference between 5- and 9-step scheme is found to be small (average correlation value of 0.96) under various oxygen concentrations. Therefore, the simulation of bench-scale experiments further suggests: (1) the 3-step scheme results in a significant inaccuracy; (2) the 9-step scheme is excessively complex; and (3) the 5-step scheme is the best compromise, since it is relatively simple but still adequate to accurately reproduce experiments. Therefore, the 5-step scheme is used in all following simulations.

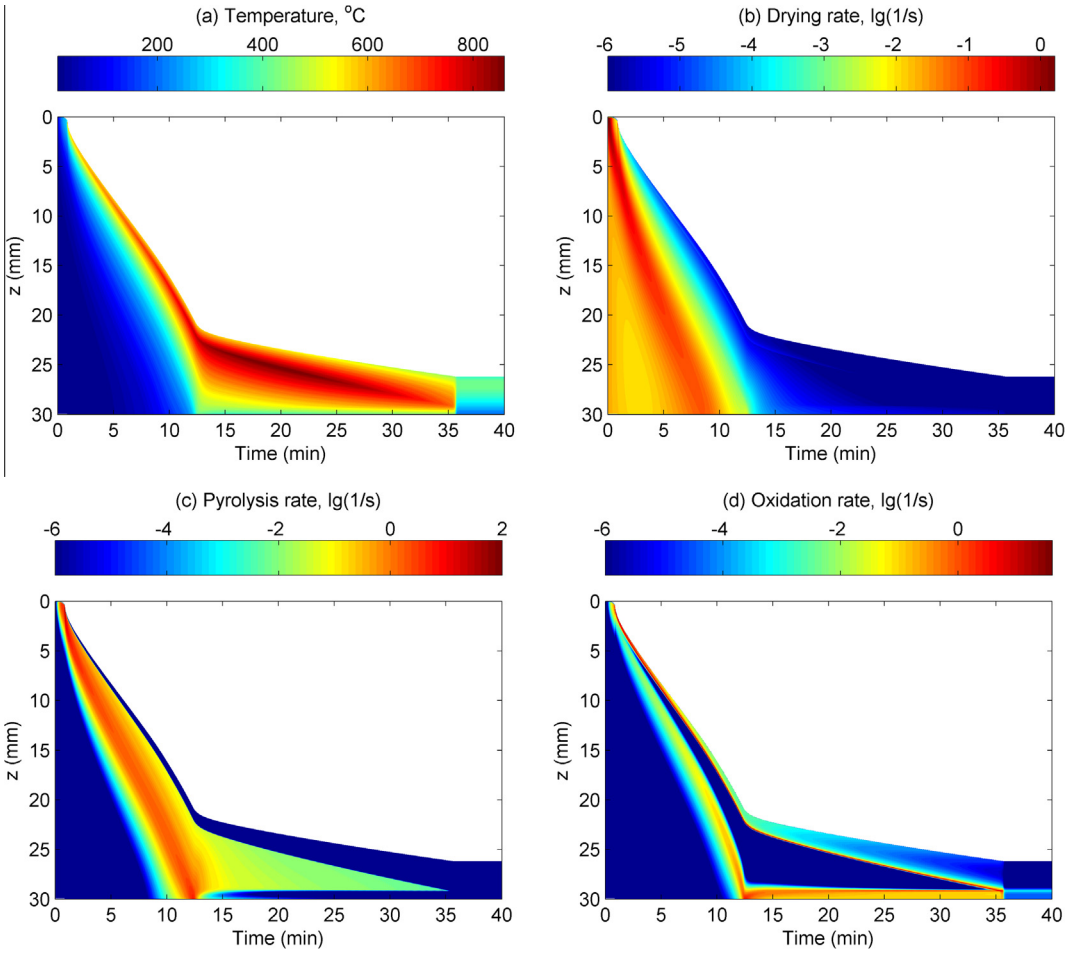

Fig. 4. Predicted contours in depth vs. time of: (a) temperature, (b) drying rate, (c) pyrolysis rate, and (d) oxidation rate, for the bench-scale peat experiment in air under an irradiation $\dot{q}''_e = 20$ kW/m^2 during the entire experiment.

Since the species conductivity (k_i), heat capacity (c_i), and heat of reactions (h_k) are selected from the literature, appreciable uncertainties exist in these parameters. In order to study the sensitivity of these input parameters, their variation ranges are selected from the literature (see Table 4), and an stochastic sensitivity analysis is conducted. Six parameters, $k_{sp}, k_{sc}, c_p, \Delta H_{pp}, \Delta H_{O_2}$, and $h_{m,0}$ are sampled randomly and combined to conduct many simulations and study their sensitivity.

4.3. Modeling results

Fig. 4 shows the predicted evolution of the temperature and reaction-rate profiles for the experiment under irradiation of 20 kW/m^2 for the entire experiment. The modeling results show that the peak temperature quickly increases to 550 °C within 1 min (Fig. 4a) because oven-dried peat only has a small amount of water (MC ≈ 10%) (Huang and Rein, 2014) and thus a weak endothermic contribution from drying (Fig. 4b). This shows that a successful ignition can be simulated with 1 min irradiation, agreeing with the experiment in Hadden (2011). Then, the temperature continues to increase as the rate of char oxidation increases, while the rate of pyrolysis weakens and widens.

After about 12 min, both the thermal front (Fig. 4b) and the multi-layer smouldering front (Fig. 4b–d) reach the bottom. At this moment, a second forward char oxidation front is started, fed by oxygen diffusion through the porous bottom wall (Fig. 4d), which increases the temperature and results in a second peak in mass-loss rate curve (Figs. 3 and 5b). Same as the experimental observation in Hadden (2011), all organic content is consumed by the end, and only mineral ash is left.

Fig. 5a and b compares the mass-loss rate between experiment and predictions at both N_2 (X_{O_2} = 0%) and air (X_{O_2} = 21%) atmospheres. In N_2 (Fig. 5a), the predicted mass-loss rate shows only one peak, and gives an excellent agreement with experiment. In order to test the modeling sensitivity to physico-chemical properties, 40 runs of stochastic sampling for four parameters (k_{sp}, k_{sc}, c_p, and ΔH_{pp}) are conducted. Then, 40 stochastic mass-loss rate curves are shown by a shadow region in Fig. 5a. Most of experimental date is included in the shadow region, hence validating the model predictions. The thin shadowed region for the predictions in Fig. 5a shows that the process under N_2 is weakly sensitive to these four parameters.

In air (Fig. 5b), the model predicts the same two-peaks mass-loss rate curve as experiment, although the overall agreement is not as high as for the N_2 case. Modeling reveals that when the thermal and oxidation reactions reach the bottom, the second peak occurs because of the initiation of a forward char oxidation (Fig. 4b). Another group of four parameters (k_{sp} $c_p, \Delta H_{O_2}$ and h_{m0}) are selected for a similar stochastic sensitivity analysis. Modeling generates a similar shadow region, which also includes most of experimental data, implying the validation of the model also for oxidative atmospheres. The shadow region is wider than the N_2 case, showing the prediction in the oxidative atmosphere is more sensitive to variations of the selected parameters. Particularly, values of h_{m0} (relating to oxygen supply) and ΔH_{O_2} (relating to overall heat of reaction) are found to affect modeling results,

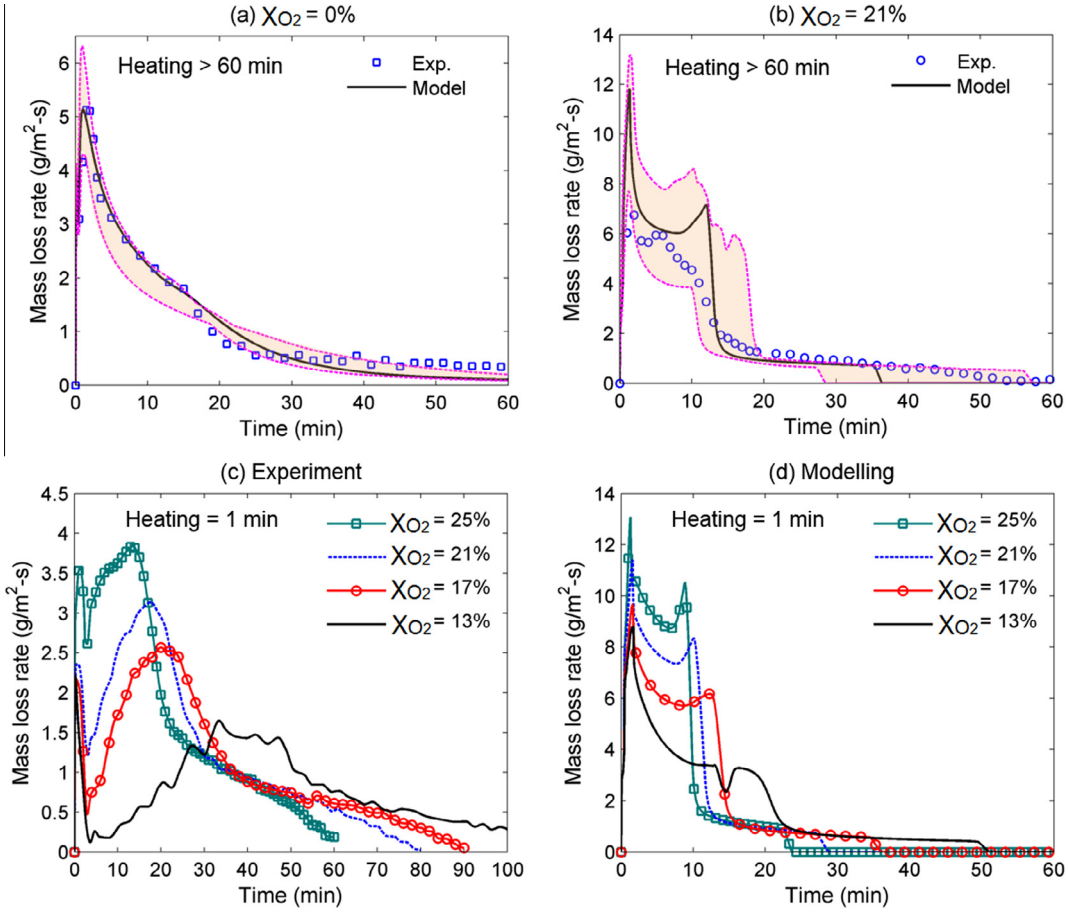

Fig. 5. Comparison of bench-scale mass-loss rate between measurements in Hadden (2011) and predictions at (a) N_2 (X_{O_2} = 0%), and (b) air (X_{O_2} = 21%) under $\dot{q}''_e = 20$ kW/m^2 during entire experiment. The shadow shows sensitivity from stochastic sampling. Qualitative comparison for the ignition protocol of $\dot{q}''_e = 20$ kW/m^2 for 1 min, between (c) measurements Hadden et al. (2013), and (d) predictions.

especially changing the magnitude of the peak of mass-loss rate and smouldering duration.

With the same experimental setup, Hadden et al. (2013) further conducted experiments with the irradiation of 20 kW/m^2 for a short duration of 1 min (mass-loss rates are plotted in Fig. 5c). After the irradiation, there is a clear decrease in mass-loss rate. However, as observed from their experiments, for 1 min irradiation on the top surface, only several spots were ignited, rather than producing uniform ignition. Then, the fire spread from these spots laterally over the surface, i.e. 2D spread. Such a 2D smouldering spread cannot be represented by the 1D model, so only qualitative comparison is valid for the short irradiation cases.

Fig. 5d shows the modeled mass-loss rate for these 1-min ignition experiments. In order to ensure a successful ignition under low oxygen concentration, a larger oxygen supply ($h_{m,0} = 20$ g/m^2-s) is set for the boundary condition on the top surface. Comparison shows that the model successfully predicts two peaks of all mass-loss rate curves, in agreement with experiment. Modeling also provides three outcomes as X_{O_2} increases: (1) the overall mass-loss rate increases, (2) the second peak occurs earlier; and (3) smouldering duration decreases. All three findings agree with the experimental curves in Fig. 5c. Therefore, the proposed 5-step scheme and the multi-physical 1D model show a good capability to simulate the smouldering combustion of peat at various oxygen concentrations.

5. Conclusions

The thermochemical conversion of peat in smouldering combustion by combining experiments and modeling is investigated at both thermogravimetric and bench scales under various oxygen concentrations. Three kinetic schemes are explored. Excellent balance between accuracy and complexity is found in the 5-step scheme which includes drying, one pyrolysis and three oxidations. The influence of oxygen is found to be weaker than the first order previously assumed in the literature. This is the first time that the influence of oxygen on biomass smouldering is explained in terms of both chemistry and transport phenomena across scales.

Acknowledgements

The authors thank Prof. Haixiang Chen (University of Science and Technology of China) for valuable discussions and providing TG data of moss peat. Valuable comments from Dr. Rory Hadden (University of Edinburgh), Dr. Albert Simeoni (Exponent, Inc.), Dr. Salvador Navarro-Martinez and Francesco Restuccia (Imperial College London) are acknowledged.

Appendices A and B

A.1. Conversion of kinetic parameters

In this section, the conversion of kinetic parameters when choosing different mass action functions, i.e. $f(m_A^*)$ in Eq. (16), is presented. The mass action function quantifies the conversion degree of A using the virtual peak mass of the reactant as characteristic. Both $\dot{\omega}_k$ and m_A could be normalized to a different characteristic mass, for example, FDS, ThermaKin, and Rein et al. (2006) normalize to the initial cell mass (m_0) as

$$\begin{cases} \left(\dot{\omega}_k^*\right)' & = Z_k' e^{-E_k/RT}\left[\left(m_A^*\right)'\right]^{n_k} f(Y_{O_2}) \\ \left(m_A^*\right)' & = \frac{m_A}{m_0} \end{cases} \quad (A.1)$$

Since the actual destruction rate of A in Eq. (A.1) is always the same regardless the selection of mass action function, $\dot{\omega}_{dA_k} = m_{sA,0}\dot{\omega}_k^* = m_0(\dot{\omega}_k^*)'$, E_k and n_k are independent of the chosen characteristic mass, and a simple conversion exists between their pre-exponential factor as

$$Z_k' = Z_k\left(\frac{m_{sA,0}}{m_0}\right)^{1-n_k} = Z_k(Y_{sA,0})^{1-n_k}. \quad (A.2)$$

where $Y_{sA,0} = m_{sA,0}/m_0$ is the initial mass fraction of source species for A in the cell. Similar simple conversion may also exist when normalized to some other characteristic mass.

Table B1
Kinetic parameters for the low-mineral moss peat and high-mineral forest peat samples with the 9-step scheme. $\Delta H > 0$ (endothermic); $\Delta H < 0$ (exothermic). The parameters for drying are listed in Table 1.

	Moss peat	Range	Forest peat	Range	Unit
Y_{h0}	20.1	[19.9, 22.6]	30.9	[17.8, 31.5]	
Y_{c0}	17.4	[17.3, 24.6]	10.8	[9.8, 15.8]	%
Y_{l0}	61.7	[54.9, 62.1]	58.3	[57.1, 68.7]	
$\lg A_{hp}$	6.95	[5.29, 7.20]	8.91	[8.91, 15.6]	lg(s^{-1})
E_{hp}	93.8	[78.5, 96.5]	111	[111, 170]	kJ/mol
n_{hp}	0.98	[0.74, 1.00]	1.98	[0.98, 2.37]	–
$\nu_{\alpha,hp}$	0.16	[0.15, 0.25]	0.14	[0.13, 0.68]	kg/kg
ΔH_{hp}	0.5	–	0.5	–	MJ/kg
$\lg A_{cp}$	11.7	[9.43, 12.9]	13.6	[11.7, 14.9]	lg(s^{-1})
E_{cp}	156	[131, 168]	183	[159, 199]	kJ/mol
n_{cp}	1.00	[0.88, 1.13]	1.61	[0.99, 1.28]	–
$\nu_{\alpha,cp}$	0.03	[0.03, 0.04]	0.39	[0.25, 0.43]	kg/kg
ΔH_{cp}	0.5	–	0.5	–	MJ/kg
$\lg A_{lp}$	10.9	[10.1, 12.5]	12.7	[11.6, 14.7]	lg(s^{-1})
E_{lp}	142	[135, 158]	174	[161, 185]	kJ/mol
n_{lp}	7.07	[6.20, 8.10]	6.64	[6.22, 7.34]	–
$\nu_{\alpha,lp}$	0.37	[0.37, 0.41]	0.55	[0.36, 0.57]	kg/kg
ΔH_{lp}	0.5	–	0.5	–	MJ/kg
$\lg A_{ho}$	20.2	[15.0, 20.2]	4.17	[4.17, 5.75]	lg(s^{-1})
E_{ho}	294	[228, 295]	86.1	[69.8, 87.6]	kJ/mol
n_{ho}	0.47	[0.40, 1.60]	2.75	[1.71, 2.75]	–
$n_{O_2,ho}$	0.11	[0.10, 0.13]	0.95	[0.90, 1.30]	–
$\nu_{\beta,ho}$[a]	0.30	[0.30, 0.56]	0.12	[0.10, 0.14]	kg/kg
ΔH_{ho}	−20.9	–	−26.2	–	MJ/kg
$\lg A_{co}$	24.2	[20.4, 25.4]	7.17	[6.15, 7.47]	lg(s^{-1})
E_{co}	278	[236, 297]	70.6	[66.3, 91.6]	kJ/mol
n_{co}	1.73	[1.00, 1.97]	3.07	[2.15, 3.12]	–
$n_{O_2,co}$	0.74	[0.72, 0.91]	0.98	[0.91, 1.21]	–
$\nu_{\beta,co}$[a]	0.06	[0.72, 0.91]	0.34	[0.31, 0.51]	kg/kg
ΔH_{co}	−28.2	–	−19.8	–	MJ/kg
$\lg A_{lo}$	23.9	[20.6, 24.5]	6.59	[5.30, 6.58]	lg(s^{-1})
E_{lo}	289	[254, 299]	97.5	[79.9, 97.5]	kJ/mol
n_{lo}	4.01	[2.79, 4.16]	1.09	[0.93, 1.38]	–
$n_{O_2,lo}$	0.93	[0.91, 1.08]	0.93	[0.82, 1.01]	–
$\nu_{\beta,lo}$[a]	0.70	[0.68, 0.77]	0.48	[0.44, 0.56]	kg/kg
ΔH_{lo}	−9.7	–	−15.5	–	MJ/kg
$\lg A_{\beta o}$	7.64	[6.89, 8.2]	17.8	[17.0, 21.0]	lg(s^{-1})
$E_{\beta o}$	120	[110, 127]	231	[203, 269]	kJ/mol
$n_{\beta o}$	1.25	[1.08, 1.45]	3.58	[3.53, 4.64]	–
$n_{O_2,\beta o}$	0.89	[0.74, 0.95]	0.87	[0.53, 0.87]	–
$\nu_{a,\beta o}$	0.04	[0.03, 0.04]	0.67	[0.59, 0.75]	–
$\Delta H_{\beta o}$	−28.8	–	−9.8	–	MJ/kg
$\lg A_{\alpha o}$	12.2	[10.6, 12.8]	19.0	[15.3, 19.9]	lg(s^{-1})
$E_{\alpha o}$	177	[159, 186]	243	[202, 253]	kJ/mol
$n_{\alpha o}$	0.93	[0.75, 0.99]	1.59	[1.26, 1.82]	–
$n_{O_2,\alpha o}$	0.52	[0.50, 0.64]	0.92	[0.87, 1.04]	–
$\nu_{a,\alpha o}$	0.08	[0.07, 0.08]	0.59	[0.57, 0.64]	kg/kg
$\Delta H_{\alpha o}$	−27.8	–	−12.4	–	MJ/kg

[a] Calculated from Eq. (12).

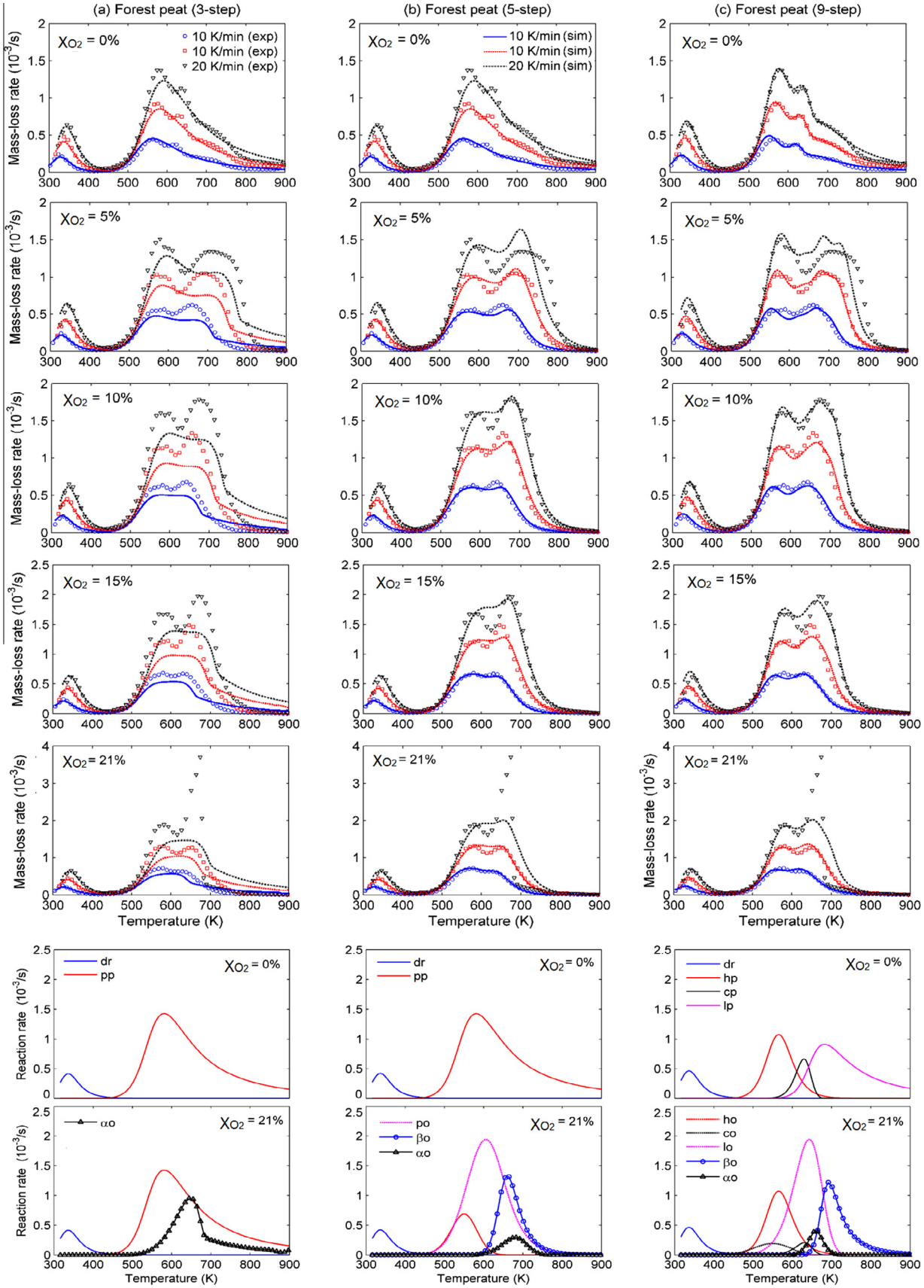

Fig. B1. Measured and predicted DTG curves, and predicted reaction rates of the high-mineral forest peat under different oxygen concentrations (X_{O_2}) (Zhao et al., 2014) by (a) 3-step, (b) 5-step, and (c) 9-step kinetic schemes.

B.1. Predicting TG data of peat sample with high mineral content

The second soil sample was collected from the wild forest of Changpai Mountains in Northeast China (forest peat soil) with a high mineral content (IC ≈ 22%). The sample was pulverized into powders and dried at 80 °C for 24 h. A SDT Q600 TG-DSC thermal analyzer was used to record both the mass-loss (previously reported in Zhao et al. (2014)) and heat-flow curves. The initial mass of peat was about 5 mg for all experiments. In each experiment, the TG temperature was increased from 298 K to 1100 K at three heating rates of 10, 20, 30 K/min. Five oxygen concentrations were selected, 0% (nitrogen), 5%, 10%, 15% and 21% (air). Therefore, in total 15 sets of TG data are available: 5 oxygen concentrations × 3 heating rates. The designed atmosphere flow rate was 50 mL/min at the atmospheric pressure and the room temperature. The uncertainty of two repeating TG tests is within 2%, showing a good repeatability.

12 sets are chosen for optimization, and another 3 sets: (1) $X_{O_2} = 0\%$ at 10 K/min, (2) $X_{O_2} = 10\%$ at 20 K/min, and (3) $X_{O_2} = 21\%$ at 30 K/min for blind predictions. The best values found for the parameters are listed in Tables 1 (3- and 5-step) and B1 (9-step), respectively. The overall errors in both the optimization and blind prediction for each kinetic scheme can be found in Table 2. The measured and predicted TG curves of all mass-loss rates and reaction rates (20 K/min) in $X_{O_2} = 0\%$ and 21% are shown in Fig. B1. Similar to the low-mineral peat samples of Fig. 2, 5- and 9-step kinetic schemes give a better prediction than the 3-step kinetic scheme. Note that the exceptionally high second peak in DTG curve ($X_{O_2} = 21\%$) is probably due to the uncertainty of TG experiment.

References

Amutio, M., Lopez, G., Aguado, R., Artetxe, M., Bilbao, J., Olazar, M., 2012. Kinetic study of lignocellulosic biomass oxidative pyrolysis. Fuel 95, 305–311.

Anca-Couce, A., 2016. Reaction mechanisms and multi-scale modelling of lignocellulosic biomass pyrolysis. Prog. Energy Combust. Sci. 53, 41–79.

Anca-Couce, A., Zobel, N., Berger, A., Behrendt, F., 2012. Smouldering of pine wood: kinetics and reaction heats. Combust. Flame 159, 1708–1719.

Bal, N., Rein, G., 2013. Relevant model complexity for non-charring polymer pyrolysis. Fire Saf. J. 61, 36–44.

Belcher, C.M., Yearsley, J.M., Hadden, R.M., McElwain, J.C., Rein, G., 2010. Baseline intrinsic flammability of Earths ecosystems estimated from paleoatmospheric oxygen over the past 350 million years. Proc. Nat. Acad. Sci. 107, 22448–22453.

Bergner, K., Albano, C., 1993. Thermal analysis of peat. Anal. Chem. 65, 204–208.

Carvalho, E.R., Veras, C.A.G., CarvalhoJr, J.A., 2002. Experimental investigation of smouldering in biomass. Biomass Bioenergy 22, 283–294.

Cozzani, V., 2000. Reactivity in oxygen and carbon dioxide of char formed in the pyrolysis of refuse-derived fuel. Ind. Eng. Chem. Res. 39, 864–872.

Di Blasi, C., 1993. Modeling and simulation of combustion processes of charring and non-charring solid fuels. Prog. Energy Combust. Sci. 19, 71–104.

Di Blasi, C., 2008. Modeling chemical and physical processes of wood and biomass pyrolysis. Prog. Energy Combust. Sci. 34, 47–90.

Di Blasi, C., Branca, C., Teislev, B., 2004. Development of a novel reactor for the oxidative degradation of straw. Bioresour. Technol. 91, 263–271.

Ding, Y., Wang, C., Chaos, M., Chen, R., Lu, S., 2016. Estimation of beech pyrolysis kinetic parameters by Shuffled Complex Evolution. Bioresour. Technol. 200, 658–665.

Hadden, R.M., (2011). Smouldering and Self-Sustaining Reactions in Solids: An Experimental Approach (Ph.D. thesis). University of Edinburgh.

Hadden, R.M., Rein, G., Belcher, C.M., 2013. Study of the competing chemical reactions in the initiation and spread of smouldering combustion in peat. Proc. Combust. Inst. 34, 2547–2553.

Holman, J., 1989. Heat Transfer. Mechanical Engineering Series. McGraw-Hill.

Huang, X., Rein, G., 2014. Smouldering combustion of peat in wildfires: inverse modelling of the drying and the thermal and oxidative decomposition kinetics. Combust. Flame 161, 1633–1644.

Huang, X., Rein, G., 2015. Computational study of critical moisture and depth of burn in peat fires. Int. J. Wildland Fire 24, 798–808.

Huang, X., Rein, G., Chen, H., 2015. Computational smoldering combustion: predicting the roles of moisture and inert contents in peat wildfires. Proc. Combust. Inst. 35, 2673–2681.

Huggett, C., 1980. Estimation of rate of heat release by means of oxygen consumption measurements. Fire Mater. 4, 61–65.

Jacobsen, R., Lemmon, E., Penoncello, S., Shan, Z., Wright, N., 2003. Thermophysical properties of fluids and materials. In: Bejan, A., Kraus, A. (Eds.), Heat Transfer Handbook. John Wiley & Sons, pp. 43–159, chapter 2.

de Jonge, H., Mittelmeijer-Hazeleger, M.C., 1996. Adsorption of CO2 and N2 on soil organic matter: nature of porosity, surface area, and diffusion mechanisms. Environ. Sci. Technol. 30, 408–413.

Lautenberger, C., Fernandez-Pello, C., 2009. Generalized pyrolysis model for combustible solids. Fire Saf. J. 44, 819–839.

Li, K.-Y., Huang, X., Fleischmann, C., Rein, G., Ji, J., 2014. Pyrolysis of medium-density fiberboard: optimized search for kinetics scheme and parameters via a Genetic Algorithm driven by Kissingers method. Energy Fuels 28, 6130–6139.

McKendry, P., 2002. Energy production from biomass (part 1): overview of biomass. Bioresour. Technol. 83, 37–46, Reviews Issue.

Moussa, N., Toong, T., Garris, C., 1977. Mechanism of smoldering of cellulosic materials. Symp. (Int.) Combust. 16, 1447–1457.

Niu, H., 2014. Pyrolysis Kinetics and Flammability Study of Forest Fuels (Ph.D. thesis). Unversity of Science and Technology of China.

Ohlemiller, T., 1985. Modeling of smoldering combustion propagation. Prog. Energy Combust. Sci. 11, 277–310.

Punmia, B., Jain, A., 2005. Soil Mechanics and Foundations. Laxmi Publications Pvt Limited.

Rein, G., 2013. Smouldering fires and natural fuels. In: Belcher, C. (Ed.), Fire Phenomena and the Earth System. Wiley and Sons, pp. 15–33, chapter 2.

Rein, G., 2016. Smoldering combustion. In: Hurley, M.J., Gottuk, D.T., Hall, J.R., Jr, Harada, K., Kuligowski, E.D., Puchovsky, M., Torero, J.L., Watts, J.M., Jr, Wieczorek, C.J. (Eds.), SFPE Handbook of Fire Protection Engineering. Springer, New York, pp. 581–603.

Rein, G., Lautenberger, C., Fernandez-Pello, A.C., Torero, J.L., Urban, D.L., 2006. Application of genetic algorithms and thermogravimetry to determine the kinetics of polyurethane foam in smoldering combustion. Combust. Flame 146, 95–108.

Su, Y., Luo, Y., Wu, W., Zhang, Y., Zhao, S., 2012. Characteristics of pine wood oxidative pyrolysis: degradation behavior, carbon oxide production and heat properties. J. Anal. Appl. Pyrol. 98, 137–143.

Turetsky, M., Benscoter, B., Page, S., Rein, G., van der Werf, G.R., Watts, A., 2015. Global vulnerability of peatlands to fire and carbon loss, (invited progress paper). Nature Geoscience 8 (1), 11–14. http://dx.doi.org/10.1038/NGEO2325.

Wu, D., Huang, X., Norman, F., Verplaetsen, F., Berghmans, J., den Bulck, E.V., 2015. Experimental investigation on the self-ignition behaviour of coal dust accumulations in oxy-fuel combustion system. Fuel 160, 245–254.

Yu, F., Wei, G., Zhang, X., Chen, K., 2006. Two effective thermal conductivity models for porous media with hollow spherical agglomerates. Int. J. Thermophys. 27, 293–303.

Zhao, W., Chen, H., Liu, N., Zhou, J., 2014. Thermogravimetric analysis of peat decomposition under different oxygen concentrations. J. Therm. Anal. Calorim. 117, 489–497.